A 1-D Photonic Band Gap Tunable Optical Filter in (110) Silicon

Ariel Lipson and Eric M. Yeatman

***Abstract*—In this paper, we describe an electrostatically tunable optical bandpass filter that is fabricated in (110) silicon. Deep reactive-ion etching is the main process that is used to fabricate the overall device structure. To create the highly parallel surfaces that are needed for the photonic band gap elements, electrochemical (KOH) etching of the vertical (111) planes is then used. Back etching is used to release the moving parts. Fiber pigtails are attached in etched alignment grooves, and fiber–fiber insertion loss below 11 dB was obtained. The measured passband width was 3 nm with a tuning range of 8 nm. [2006-0165]**

***Index Terms*—Anisotropic etching, optical filter, photonic band gap (PBG), silicon-on-insulator (SOI).**

I. Introduction

THE Fabry–Pérot (FP) cavity, a resonator consisting essentially of a pair of parallel mirrors, is one of the most common structures that are used for optical filtering. One benefit of the FP cavity is that if the separation can be varied, a tunable filter results. Microelectromechanical systems (MEMS) technology provides an attractive approach to providing the mechanical tuning mechanism, thus enabling a low-cost highly integrated FP filter. In applications where a narrowly selective spectral response is required, the cavity must be highly resonant, and this, in turn, requires very reflective mirrors, as well as a high degree of mirror planarity and parallelism. An important device of interest is a tunable channel selection filter for densely multiplexed optical communication networks, where one channel (the passband) is selected from a range of channels (wavelengths) [1]. A typical requirement is for a channel width of 10–100 GHz, within an active range of 4000 GHz, corresponding to the main optical communication wavelength band of 1530–1560 nm. This demands a finesse (ratio of stopband to passband width) in the filter of several hundreds.

While some FP filters use metal-coated mirrors to achieve high reflectance, better results can be realized, without the inherent absorption loss of the metal surfaces, using a stack of alternating dielectrics. To achieve high reflectance from a dielectric stack without requiring a large number of layers, a high refractive index contrast is needed. The term photonic band gap (PBG) is widely used to describe periodic structures having such large index differences; thus, we can refer to high-contrast stacks as 1-D PBGs.

Sequential deposition on a flat substrate is the most straightforward approach to fabricating a dielectric stack, and besides being a standard method for manufacturing conventional filter plates, it has also been investigated by a number of researchers for use in tunable integrated structures. In [2], two stacks are grown by $Al_xGa_{1-x}As$ epitaxy, with x taking the values of 0.1 and 0.85. Using large numbers of pairs ($\approx$20 for each mirror), high reflectance was achieved, giving a passband width of 1 nm, and tuning was provided by rotating the released upper mirror electrostatically on a torsional suspension. Higher index contrast was achieved in [3], using Si/SiO_2 stacks of only two pairs each, to form mirrors on either side of a Si membrane. A 3-nm stopband in reflection was measured, and a modest tuning range (5.3 nm) was achieved by varying the membrane temperature rather than the mirror spacing. Even higher index contrast was reported in [4], where eight-layer stacks of Si and MgF_2 were used to fabricate an air-gap FP filter with a passband width of about 100 nm (for a center wavelength in this case of 3.5 μm). MEMS tuning of the air gap was proposed, but integration of the actuator and filter was not reported. A tunable MEMS filter is reported in [5], in which a high tuning range of 80 nm was achieved. The passband full-width at half-maximum (FWHM) is high due to the single-layer mirrors, as this is not a PBG device. Results are presented for reflection mode only.

Such multilayer filters have the significant disadvantage for integration that the input and output fibers must be mounted perpendicular to the plane of the device. They also cannot practically use air as the lower index medium in a stack, even one of a modest number of layers. Thus, integrated optical filters with the optical axis parallel to the wafer surface have been actively pursued. These fall into two categories: those where the light is confined in a waveguide, and those where the light passes through the filtering structure as a free-space beam.

Generally, the waveguide devices do not implement an FP cavity but use a single periodic section to get a filter response. This naturally requires a longer periodic section to get the same spectral discrimination. Most of the reported devices are based on III–V semiconductor heterostructures, as these offer the possibility of integrating optoelectronic functionality such as gain and high-speed modulation. However, insufficient precision in the micromachining processes of these materials leads to high optical losses, which add to the substantial coupling losses that are generally obtained by optoelectronic waveguide

Manuscript received August 6, 2006; revised December 15, 2006. This work was supported by the Engineering and Physical Sciences Research Council (U.K.). Subject Editor O. Solgaard.

A. Lipson was with Department of Electrical and Electronic Engineering, Imperial College London, SW7 2AZ London, U.K. He is now with Microsaic Systems Ltd., GU21 5BX Surrey, U.K. (e-mail: alipson@ic.ac.uk).

E. M. Yeatman is with the Department of Electrical and Electronic Engineering, Imperial College London, SW7 2AZ London, U.K. (e-mail: e.yeatman@imperial.ac.uk).

Color versions of one or more of the figures in this paper are available online at http://ieeexplore.ieee.org.

Digital Object Identifier 10.1109/JMEMS.2007.892894

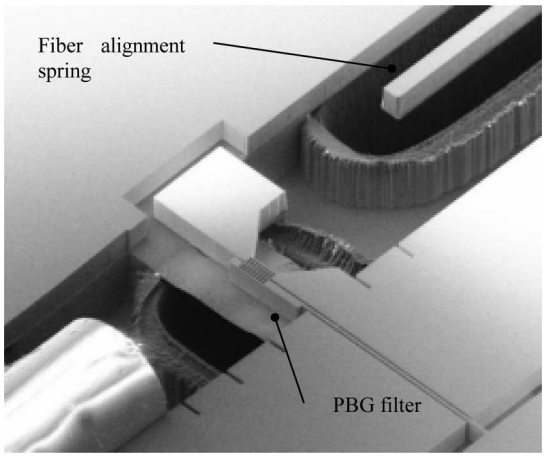

Fig. 1. SEM photograph of a tunable free-space silicon MEMS filter showing the 1-D PBG filter, input fiber, grooves, and springs. Back etching was used to release the fragile structures (some oxide is still evident).

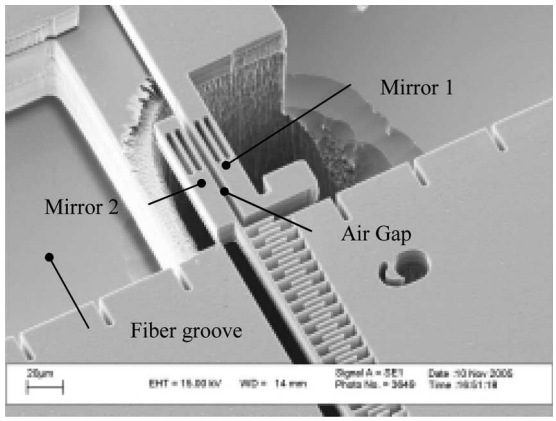

Fig. 2. Detail of tunable silicon MEMS filter showing the 1-D PBG mirrors. Tuning is achieved through electrostatic actuation.

devices when coupled to optical fiber. In [6], a static filter with passband width < 0.5 nm was achieved by etching slits in AlGaAs waveguides. Overall loss was not given, but an excess 10-dB loss was measured when compared to an equivalent waveguide without the filter section. In [7], a static filter was formed using an array of round holes in air-bridged AlGaAs waveguides, resulting in a transmission band of $\approx$4 nm. Device loss was not given, but losses in waveguide sections without the filter structure were 3–6 dB/mm. In [8], etched gratings were used as couplers in an interferometric filter that is based on InP waveguides, and tuning was achieved by current injection. In [9], a silicon waveguide was used, with etched holes forming a PBG filter, and some tuning was achieved by straining the structure. Losses were not reported.

We have developed a device using a free-space beam between input and output fibers. This avoids the high fiber–waveguide coupling losses, and its symmetry assures much lower polarization dependence. The basic structure is illustrated in Fig. 1. An FP cavity is formed between two PBG mirrors, one of which is suspended on a cantilever beam, which can be translated electrostatically to change the cavity length, and thus provide tuning. To achieve sufficient mirror quality for a high-performance device, silicon was used as the dielectric material. Previously, we reported a static (nontuning) filter that is based on this approach [10], [11], and we report here the first such device that is tuned by a MEMS mechanism.

Only three silicon–air paired layers are needed for each mirror due to the high index of refraction contrast between silicon and air. These are shown more clearly in Fig. 2. A Gaussian beam that is emitted from the input fiber is propagated through the PBG structure and collected using the output fiber. Even with such a highly compact design, some collimation is needed to limit beam spreading and to reduce the angular spectrum entering the filter. This is provided by the use of lensed fibers (Corning OptiFocus 700043) with 18-μm output beam diameter.

As part of this work, we developed a generic analysis method for propagating optical beams, Gaussian in particular, through 1-D PBG structures. This analysis method, which is summarized in [10], is noted here only for understanding of the optical results. From these simulations and other reports (see [12], for example), we learn that there are very tight tolerances on the fabrication processes, both on the dimensions of the silicon and air layers, and on their verticality and surface quality. It is apparent that an angle greater than 0.01° between the cavity mirrors yields a loss greater than 10 dB and widens the passband considerably [10], [13].

Dry etching processes alone are limited in the verticality and surface quality that they can achieve [14]. Excellent surface orientation and flatness are possible with anisotropic wet etching [15], but this is not suitable for machining the overall filter structure. For this reason, we have developed a fabrication process that is based on combined dry and wet etching, as previously used to machine high-precision molds [16]. A (110)-oriented silicon wafer is used with its vertical (111) planes perpendicular to the surface, to which the mirror surfaces are aligned. First, the pattern is etched by deep reactive-ion etching (DRIE); then, a rapid KOH wet etch is used to expose the (111) planes and remove the scalloping. Using this technique, we manage to maintain the flexibility of DRIE anisotropic etching, facilitating complex designs, and add the wet etching benefits of atomically smooth surfaces and parallel vertical planes.

By applying this process to a (110) bonded silicon-on-insulator (BSOI) wafer, a tunable version of the optical filter was devised, allowing the alteration of the transmitted wavelength. Due to the small feature size of the device, we chose back etching as the release process, although various alternatives are possible, including critical point drying and HF vapor etching. As compared to the static filter, the process had to be modified because the typical problem of DRIE notching at the boundary between the bonding oxide and the device layer caused the wet etching step to attack the mirror surfaces (see Figs. 5 and 6).

II. Optical Analysis

Fig. 2 shows our fabricated free-space MEMS filter that is based on a 1-D PBG structure. It comprises three deep-etched silicon bars on either side of the tunable cavity and an electrostatically driven cantilever. Fiber grooves are further

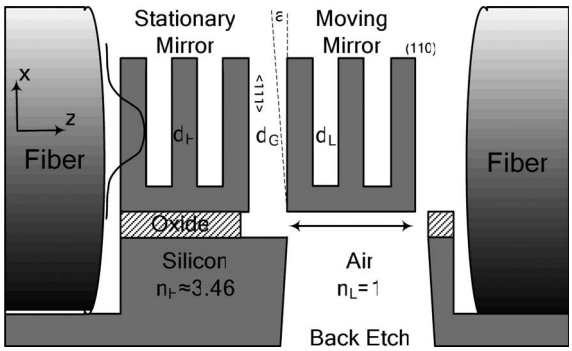

Fig. 3. Schematic of the filter assembly.

etched on either side to align the optical fibers. Fig. 3 shows the schematic of the filter assembly. A Gaussian beam emerging from the input fiber impinges on the air–silicon filter, which is characterized by the layer widths d_H, d_L, and d_G, corresponding to the silicon layer, air layer, and middle air-gap cavity. The indexes of refraction are $n_H(\lambda)$, n_L, and n_L, respectively. One side of the filter, i.e., the right mirror, is translated to enable tuning of the middle air gap and thus tuning of the filter's peak transmittance.

The following equations are used in the simulation to evaluate the experimental data. The Gaussian beam propagation before the filter is described by

$$E(x,z) = A_0 \frac{w_0}{w} \exp\left(-x^2\left[\frac{1}{w^2} - \frac{jk}{2R}\right] - j[k\cdot z + \varphi]\right) \tag{1}$$

where A_0 is the amplitude of the beam at the center, w is the radius of the beam where the amplitude drops to $1/e$, R is the radius of curvature of the surfaces of constant phase, and z is the axial distance that is measured from the beam waist (at which point $R=\infty$). w_0 is the radius of the beam at its waist. The plane-wave expansion defining this beam $[\tilde{E}_{\rm in}(\lambda,\phi)]$ is obtained using a Fourier transform.

The alternating silicon and air layers are each a quarter of a wavelength in width (or an odd multiple, $m_{\rm si}$ and $m_{\rm air}$), where the wavelength is the center wavelength of the transmitted passband (λ_c), in the respective medium ($\lambda_c = 1.55$ μm in air). The middle air-gap cavity is chosen to be half the wavelength (or a multiple, $m_{\rm cavity}$). We assign the notation $m=[m_{\rm si}, m_{\rm air}, m_{\rm cavity}, n_{\rm bars}]$ to describe the layers' $(1/4)\lambda$ multiplication factors and the number of silicon bars in each mirror. The layers' widths are determined using

$$\begin{aligned} d_H &= \frac{1}{4}\cdot m_{\rm si}\cdot\frac{\lambda_c}{n_{\rm si}} \\ d_L &= \frac{1}{4}\cdot m_{\rm air}\cdot\frac{\lambda_c}{n_{\rm air}}, \qquad m=1,3,5\ldots \\ d_G &= \frac{1}{4}\cdot m_{\rm cavity}\cdot\frac{\lambda_c}{n_{\rm air}}, \qquad m=2,4,6\ldots. \end{aligned} \tag{2}$$

For the fabricated device, $m=[21,5,4,3]$. The filter is defined using the transfer matrix formulation, where propagation through each layer is described by a 2×2 matrix [17], i.e.,

$$M_j = \begin{pmatrix} a_{11} & a_{12} \\ a_{22} & a_{22} \end{pmatrix} = \begin{pmatrix} \cos(\delta_j) & \frac{i}{\eta_j}\sin(\delta_j) \\ i\eta_j\cdot\sin(\delta_j) & \cos(\delta_j) \end{pmatrix}. \tag{3}$$

The phase is defined as

$$\delta_j = k\cdot n_j\cdot d_j\cdot\cos(\phi_j) \tag{4}$$

$$\eta_j = n_j\cos\,\phi_j, \qquad \text{for s-polarization (TE)}$$

$$\eta_j = \frac{n_j}{\cos\,\phi_j}, \qquad \text{for p-polarization (TM)} \tag{5}$$

where $k=2\pi/\lambda$ is the wavenumber, and n_j and d_j are the index of refraction and thickness of the jth layer, respectively. ϕ_j is the angle of incidence within the layer, which is calculated using Snell's law.

The transfer function of the complete multilayered system is given by the matrix product of all the characteristic matrices. The reflection and transmission coefficients, i.e., r and t, respectively, are directly calculated from the matrix subelements

$$\begin{aligned} r(\lambda,\phi) &= \frac{a_{21}+ia_{11}-ia_{22}+a_{12}}{a_{21}+ia_{11}+ia_{22}+a_{12}} \\ t(\lambda,\phi) &= \frac{-2i}{-a_{21}+ia_{11}+ia_{22}+a_{12}}\,. \end{aligned} \tag{6}$$

For a specific transfer function $t(\phi,\lambda)$, we can calculate the output spectrum by multiplying each component of $\tilde{E}_{\rm in}(\lambda,\phi)$ with $t(\phi,\lambda)$ to receive

$$\tilde{E}_{\rm out}(\lambda,\phi) = \tilde{E}_{\rm in}(\lambda,\phi)\cdot t(\lambda,\phi). \tag{7}$$

Furthermore, an overlap integral between the transmitted beam and output fiber is carried out to evaluate mode mismatch

$$\begin{aligned} \eta(\lambda) &= \frac{|\langle E_{\rm out}, E_{\rm fiber}\rangle|^2}{\langle E_{\rm out}, E_{\rm out}\rangle\,\langle E_{\rm fiber}, E_{\rm fiber}\rangle}, \\ \langle E_1, E_2\rangle &= \int \tilde{E}_1\tilde{E}_2^* d\phi. \end{aligned} \tag{8}$$

The overall spectrum is calculated from the output and input fields and the overlap efficiency

$$I(\lambda) = \eta(\lambda)\cdot\frac{\langle E_{\rm out}, E_{\rm out}\rangle}{\langle E_{\rm in}, E_{\rm in}\rangle}. \tag{9}$$

Since fabrication processing errors yield angled surfaces, we replace the vertical cavity with a wedge-shaped one. Using the Fizeau interferometer wedge approach, one can substitute the accumulated phase of (4) with one that reflects the effect of the wedge [18], [19]. The transmitted beam is now made up of an infinite series of components, with the pth wave having a phase, i.e.,

$$\begin{aligned} \delta_p &= 2k\cdot h\cdot\cos(\phi)\cdot\frac{\sin(p-1)\alpha}{\tan(\alpha)} \\ &\quad\times[\cos(p-1)\alpha - \tan(\alpha)\cdot\sin(p-1)\alpha] \\ h &= \rho\cdot\tan\,\alpha \end{aligned} \tag{10}$$

where h is the thickness of the wedge at height ρ from the apex.

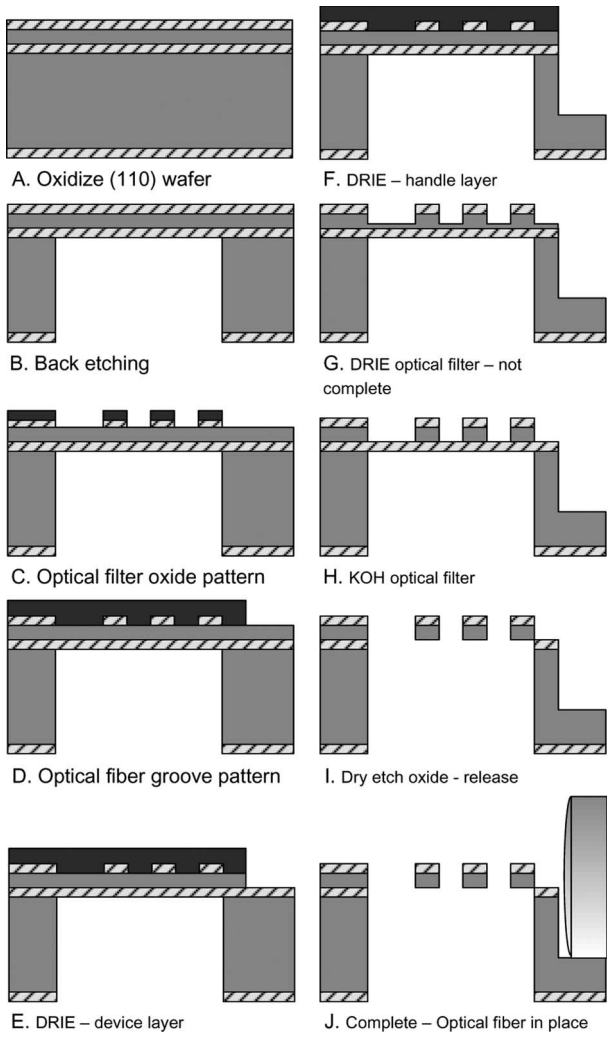

Fig. 4. Process flow for fabricating the tunable filter.

Results from this analysis method [10] indicate that for a low-loss (< 5 dB) narrow passband filter, we need better than 0.01° off-vertical etching. These are tight tolerances that are difficult to achieve with a DRIE process.

III. Fabrication

To achieve these high fabrication tolerances, we used (110)-oriented silicon wafers that have the unique ability to produce vertical trenches when properly aligned to the $\langle 111 \rangle$ flat [15]. Uenishi *et al.* have shown that optical devices with high aspect ratios can be fabricated on such wafers, and their atomically flat vertical surfaces were of very high quality, which are suitable for optical applications such as mirrors and beam splitters [13]. One drawback to this (110) wet etching technique is that any feature that is not parallel to the (111) planes will be etched in a difficult-to-foresee manner, and although there are several wet etching simulators that aid such designs, it is quite difficult to achieve controlled outcomes. Moreover, since the best practical aspect ratio [20] is $< 1:200$, we can conclude that the best etch angle will be $\vartheta = \tan^{-1}(1/200) = 0.29^\circ$, which is far from sufficient for our needs. To overcome these problems, without losing the benefit of verticality and smoothness, we used a

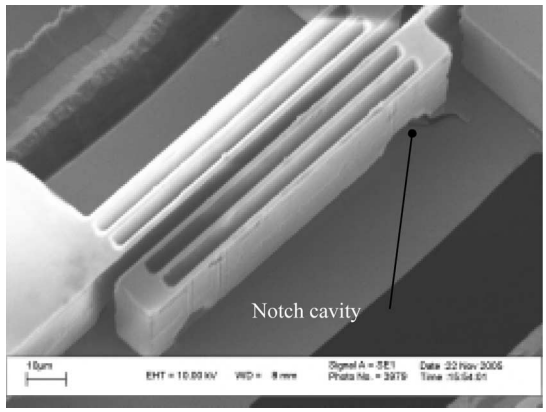

Fig. 5. Deep etching the optical filter down to the oxide layer created the usual notching effect of etching the silicon laterally close to the oxide. The effect was dramatically enhanced when placed in KOH solution.

fabrication process that is similar to that recently reported by Lee *et al.* [21], using DRIE for the initial etch followed by a short KOH wet etching process. There, the surface morphology of the vertical sidewalls was evaluated using a 3-D confocal optical profiler and scanning electron microscope (SEM). For a 70 °C, 45%, 53-s KOH etch, the surface roughness was 6.8 nm, and the off-verticality angle was $\sim 0.01^\circ$. Our process is summarized in Fig. 4. A thin layer of oxide is grown on a (110) BSOI wafer [Fig. 4(a)] and back etched for future mechanical release [Fig. 4(b)]. The back etching pattern has to be already aligned with the $\langle 111 \rangle$ flat to ensure that the next optical mask will also be aligned to the $\langle 111 \rangle$ plane. Etching the whole 420-μm depth by DRIE takes roughly 3.5 h. We use this mask to etch dicing grooves, which eliminate the need to use a dicing saw. This is required to protect the fragile devices. These etched grooves are held at several points, which are snapped out when device singulation is needed. Next, the fine optical structure is patterned using conventional photolithography onto the oxide layer after precise alignment to the $\langle 111 \rangle$ flat [Fig. 4(c)] and covered with a thick photoresist, which is then patterned to define the fiber grooves [Fig. 4(d)]. Deep etching is used to etch the grooves and springs [Fig. 4(e) and (f)].

The optical filter is then etched [Fig. 4(g)], resulting in trenches of high but still insufficient verticality. The etching goes down through the device layer, but not all the way down to the oxide, to prevent notching. If notching should occur, the next stage of KOH will create cavities and ruin the structure (see Fig. 5). The final few micrometers are etched using a 45 wt.% KOH (70 °C) solution, which smoothes out the (111) planes and makes the trenches vertical [Fig. 4(h)]. We believe that the initial DRIE etching allows the KOH to etch uniformly the whole $\langle 111 \rangle$ surface, thus giving enhanced verticality in comparison to direct wet etching, while still achieving the surface quality that is associated with the direct approach. Fig. 6 shows the outcome of KOH smoothing, eliminating scalloping and the notching cavities. It is apparent that the non-(111) planes suffer an over etch, but it is not too severe. A device with small non-(111) features, such as in Fig. 2, will not survive this process. This is why we have focused primarily on the parallel-plate capacitor actuator. Finally, the bonding oxide layer is removed from the

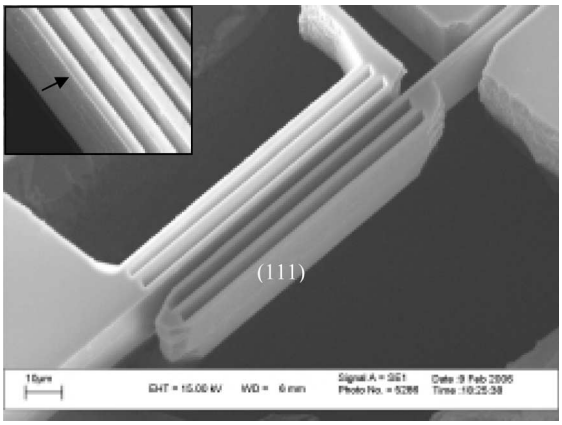

Fig. 6. DRIE of the filter was terminated 1–2 μm before the oxide layer, and etching was completed with KOH. No cavities are apparent. The effect of KOH on non-(111) planes is also apparent. Inset shows that the outer bar is over-etched and smaller in width.

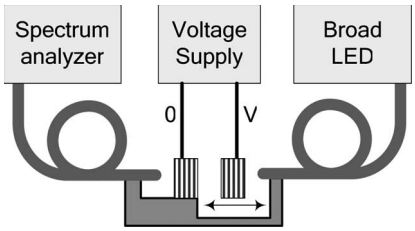

Fig. 7. Schematic of experimental setup. A broadband LED source with 1550-nm peak and 100-nm-wide spectral width is fed into a single-mode fiber. The fiber has a lens at the end creating a 9-μm-radius Gaussian beam impinged upon the optical filter. The gap between the two mirrors is tuned using a voltage supply, and the light is collected in the output fiber and measured using an Agilent 86140B spectrum analyzer.

back to completely release the structure [Fig. 4(i)], revealing the final device [Fig. 4(j)].

IV. Optical Results

Several devices were fabricated using the aforementioned process and measured using a light-emitting diode (LED) broadband source and a spectrum analyzer. Although we did not deposit metalizations for electrical contacts, direct contact between probes and silicon gave adequate contact; thus, actuation voltages were applied in this way, giving mechanical movement and optical tuning. We did not sputter or evaporate gold on the final devices as even minute amounts of metal on the filter sidewalls would greatly increase the losses. Fig. 7 elaborates on the measurement scheme.

Fig. 8 shows the measured response of a tunable optical bandpass filter. While a wider passband is realized as compared to the static version of [10], nearly 10 nm of tunability is accomplished. The increase in passband width and losses at greater travel ranges are due to the creation of a wedge cavity when the mirrors start to depart. This is caused by the cantilevered suspension of the moving mirror, which results in some small rotation when actuated, and can be removed by the use of a doubly supported suspension. Also, any inaccuracy in the physical widths of the mirror segments will create excess spectral width.

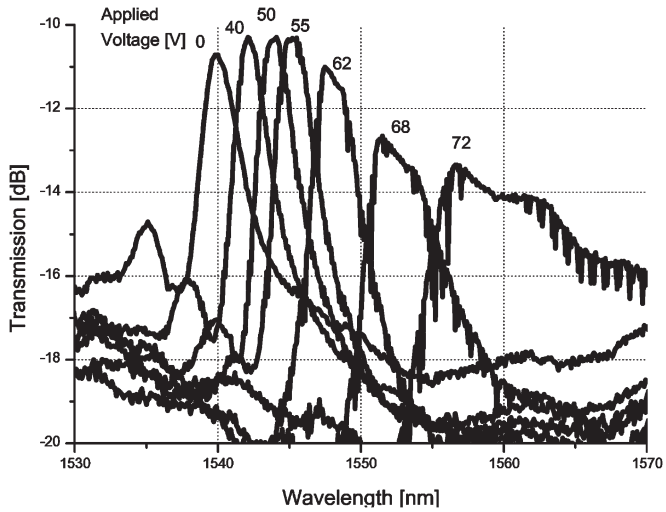

Fig. 8. Experimental measurements for tunable optical bandpass filter.

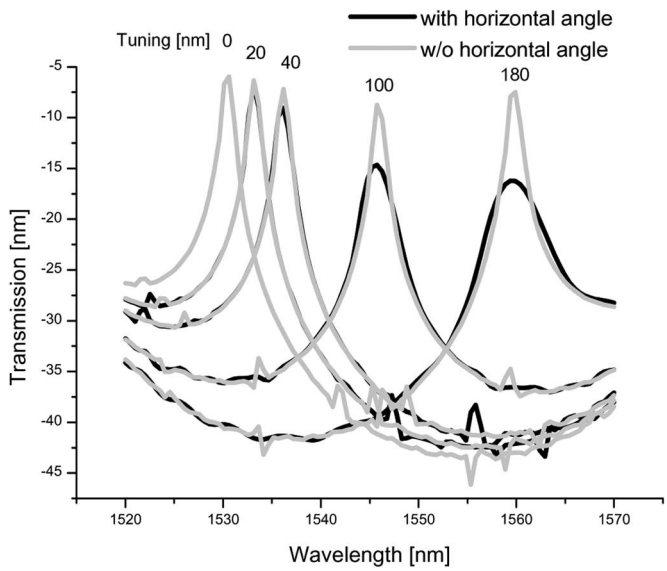

Fig. 9. Simulation results using the Fizeau interferometer approach and off-normal incidence for different lateral displacements of the actuated mirror as indicated. The passband widens with tuning range due to an increasing angle of the wedge cavity.

The tunable filter layers were measured using an SEM to an accuracy of about 100 nm. The silicon bars are about 1.9 μm, and the air gap is 3.3 μm. Using this information, a simulation model was constructed assuming an etch angle of 0.01°, which gave a reasonable starting point. Since the current design of the tunable filter is based on one fixed mirror and one on a cantilever, as the mirror moves, an angle is introduced in the horizontal plane, which increases with the tuning distance. With a known cantilever length of 100 μm, the horizontal angle can be calculated and added to the etched angle as a sum of two vectors $\alpha^2_{\text{total}} = \alpha^2_{\text{etch}} + \alpha^2_{\text{tune}}$. Fig. 9 shows how tuning effects the passband width and transmission losses due to the increase in the total angle. This corresponds well with the measured data. Note that for the maximum lateral displacement of 180 nm that is indicated, the induced mirror rotation is about 0.1°.

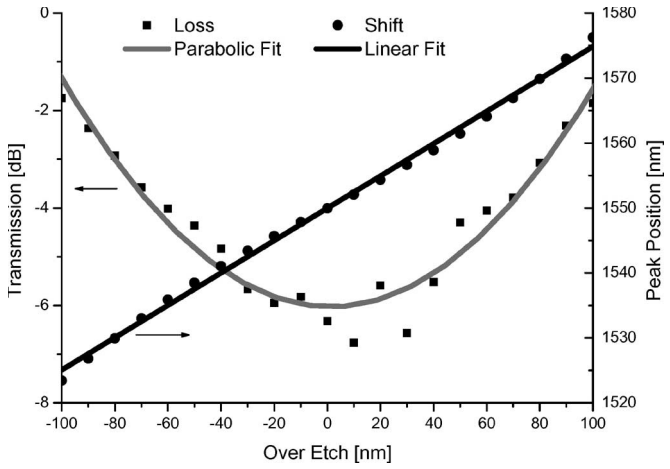

Fig. 10. Simulation of the effects of a systematic error in the silicon bars' widths. Larger errors yield lower loss and shift in the peak position.

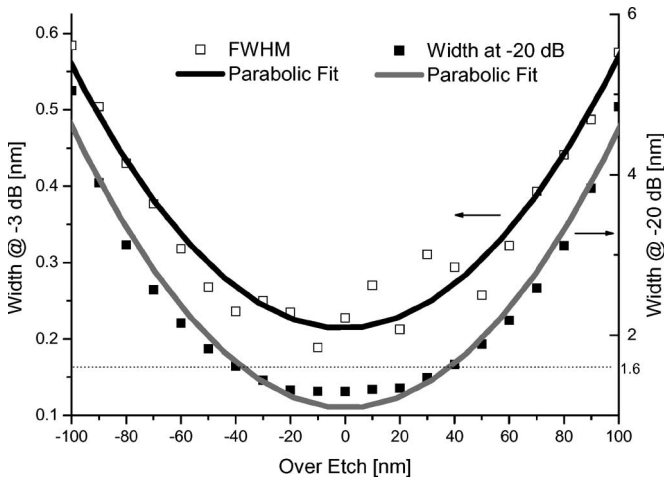

Fig. 11. Simulation of the effects of a systematic error in the silicon bars' widths. The larger the error, the wider is the passband. Widths are measured at -3 and -20 dB.

V. Fabrication Tolerances

As noted, errors in the widths of the silicon bars will create changes in the output spectra. Using the optical simulation, we analyzed the tolerances for our process, i.e., bars with a width on the order of 2 μm, with $m = [21, 5, 2, 3]$ according to the notation of Section II. We first analyzed a systematic error, i.e., all bars having the same error in width. It is important to emphasize that if a silicon bar is reduced in width, the two air gaps around it gain each half of the error width. Fig. 10 shows the results for this study. The measured loss is fiber-to-fiber loss, which is defined as the difference in transmittance between input and output fibers, with and without the device being inserted. The losses actually decrease as the error increases in a parabolic form that is centered at zero error. There is also an apparent linear shift in the position of the peak. While lower loss appears beneficial, it actually arises from a lower quality factor cavity, and therefore, we should expect a wider passband as well. Fig. 11 shows that the widths of the passband at -3 dB (FWHM) and -20 dB (channel spacing) increase rapidly with

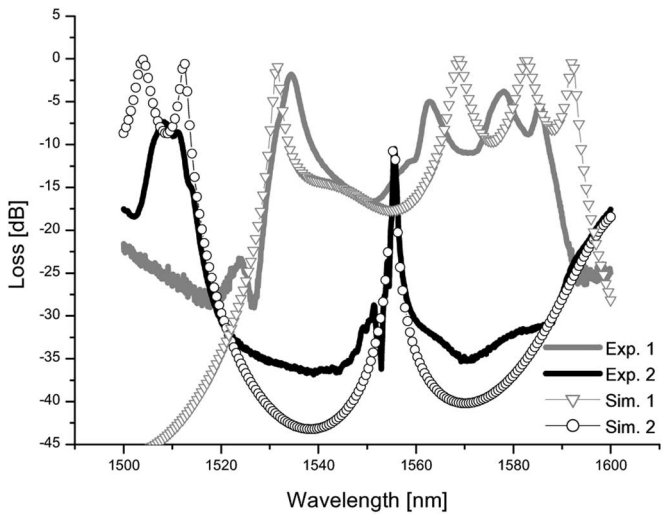

Fig. 12. Effects of over etching. Solid lines are experimental data, whereas dotted lines are simulation data. Exp. 2 is the same filter as in Exp. 1, but silicon bars are 100 nm narrower.

the error. A typical 200-GHz channel selection filter needs a 1.6-nm width at -20 dB, which means that errors must not exceed 40 nm. This tolerance will decrease, of course, with the multiplication factor m of the filter.

The systematic error was compared to the experimental results that are shown in Fig. 12. A deliberate error of 100 nm was created in one filter, and the spectra were compared: Simulation results match well the shift in position and decrease in loss. The width of the passband also seems to match very well. An even better comparison between experimental and simulated data was achieved by further correcting the measured dimensions of the layers. One notices in the inset of Fig. 6 that the last silicon bars on either end of the filter are slightly over-etched in comparison to the rest of the layers. This is typical for a DRIE as the process is very mask dependent. Therefore, on top of the systematic 100-nm over etch, we added 50 nm to the last layers, thus improving the correlation. In the next mask iteration, this problem will be eliminated by placing dummy layers that fall off when released.

In regard to random noise, we simulated many filters with errors on each bar of a certain standard deviation (STD). In a normal distribution, about 68% of the values are within one STD of the mean, and about 95% of the values are within two STDs of the mean. This means that running the simulation on 100 filters with an error of 10-nm STD will yield about 68 filters with errors of ± 10 nm. We measured how many of these filters will be acceptable for a 200-GHz filter, i.e., having a -20-dB passband smaller than 1.6 nm (optical). Fig. 13 shows the results of this simulation. It is apparent that if the random error has an STD of 10 nm, all filters will be suitable for use. A 30-nm STD decreases the yield to 30%, whereas a 50-nm STD drops the yield to merely 5%.

VI. Conclusion

In this paper, we have shown a fabricated and characterized tunable PBG optical filter for dense wavelength-division

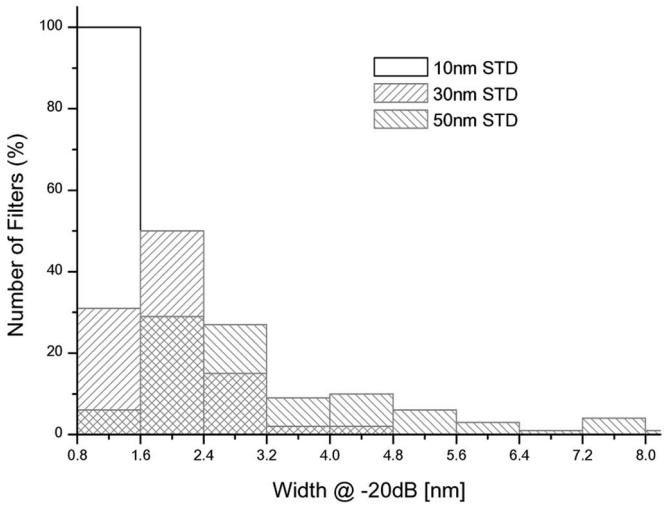

Fig. 13. Random error in the filter bars' widths. A 10-nm STD in error yields 100% usable filters, but a 50-nm STD drops the yield down to 5%.

multiplexing applications. The in-plane design facilitates the assembly of optical fibers and the construction of a mechanical tuning actuator. A reasonable 20 nm of tunability was achieved. The increase in passband width is mainly attributed to the errors in width and angle, and therefore, a study of the appropriate tolerances was presented. It appears that for a 2-μm bar process, an accuracy of at least 30 nm is needed for a 30% yield. Also, at least 0.01° verticality accuracy is needed for low-loss devices.

ACKNOWLEDGMENT

The authors would like to thank Prof. R. de la Rue for his help in fabrication.

REFERENCES

[1] D. Sadot and E. Boimovich, "Tunable optical filters for dense WDM networks," *IEEE Commun. Mag.*, vol. 36, no. 1/2, pp. 50–55, Dec. 1998.

[2] C. F. R. Mateus, C.-H. Chang, L. Chrostowski, S. Yang, D. Sun, R. Pathak, and C. J. Chang-Hasnain, "Widely tunable torsional optical filter," *IEEE Photon. Technol. Lett.*, vol. 14, no. 6, pp. 819–821, Jun. 2002.

[3] D. Hohlfeld, M. Epmeier, and H. Zappe, "A thermally tunable, silicon-based optical filter," *Sens. Actuators A, Phys.*, vol. A103, no. 1, pp. 93–99, Jan. 2003.

[4] R. H. Trimm, E. J. Tuck, G. Tuck, M. C. Buncick, M. Kranz, P. Reiner, M. G. Temmen, and P. R. Ashley, "Dynamic MEMS-based photonic bandgap filter," *IEEE Sens. J.*, vol. 5, no. 6, pp. 1451–1461, Dec. 2005.

[5] S.-S. Yun, K.-W. Jo, and J.-H. Lee, "Crystalline Si-based in-plane tunable Fabry–Pérot filter with wide tunable range," in *Proc. IEEE/LEOS Int. Conf. Opt. MEMS*, 2003, pp. 77–78.

[6] T. F. Krauss, B. Vogele, C. R. Stanley, and R. M. De La Rue, "Waveguide microcavity based on photonic microstructures," *IEEE Photon. Technol. Lett.*, vol. 9, no. 2, pp. 176–178, Feb. 1997.

[7] D. J. Ripin, K.-Y. Lim, G. S. Petrich, P. R. Villeneuve, S. Fan, E. R. Thoen, J. D. Joannopoulos, E. P. Ippen, and L. A. Kolodziejski, "One-dimensional photonic bandgap microcavities for strong optical confinement in GaAs and GaAs/Al_xO_y semiconductor waveguides," *J. Lightw. Technol.*, vol. 17, no. 11, pp. 2152–2160, Nov. 1999.

[8] T. Segawa, S. Matsuo, Y. Ohiso, T. Ishii, Y. Shibata, and H. Suzuki, "Fast tunable optical filter using cascaded Mach–Zehnder interferometers with apodized sampled gratings," *IEEE Photon. Technol. Lett.*, vol. 17, no. 1, pp. 139–141, Jan. 2005.

[9] C. W. Wong, P. T. Rakich, S. G. Johnson, M. Qi, H. I. Smith, Y. Jeon, G. Barbastathis, S.-G. Kim, E. P. Ippen, and L. C. Kimerling, "Strain-tunable silicon photonic band gap microcavities in optical waveguides," *Appl. Phys. Lett.*, vol. 84, no. 8, pp. 1242–1244, Feb. 2004.

[10] A. Lipson and E. M. Yeatman, "Low-loss one-dimensional photonic bandgap filter in (110) silicon," *Opt. Lett.*, vol. 31, no. 3, pp. 395–397, Feb. 2006.

[11] A. Lipson and E. M. Yeatman, "Free-space MEMS tunable optical filter on (110) silicon," in *Proc. Int. Conf. Opt. MEMS*, Oulu, Finland, 2005, pp. 73–74.

[12] J. Moon, "Performance limits of a micromachined tunable-cavity filter," in *Proc. Int. Conf. MSM*, 2001, pp. 278–281.

[13] Y. Uenishi, M. Tsugai, and M. Mehregany, "Micro-opto-mechanical devices fabricated by anisotropic etching of (110) silicon," *J. Micromech. Microeng.*, vol. 5, no. 4, pp. 305–312, Dec. 1995.

[14] K.-S. Chen, A. A. Ayon, X. Zhang, and S. M. Spearing, "Effect of process parameters on the surface morphology and mechanical performance of silicon structures after deep reactive ion etching (DRIE)," *J. Microelectromech. Syst.*, vol. 11, no. 3, pp. 264–275, 2002.

[15] D. L. Kendall, "Vertical etching of silicon at very high aspect ratios," in *Annual Review of Materials Science*, vol. 9. Palo Alto, CA: Annual Reviews, 1979, pp. 373–403.

[16] D. Nilsson, S. Jensen, and A. Menon, "Fabrication of silicon molds for polymer optics," *J. Micromech. Microeng.*, vol. 13, no. 4, pp. 57–61, 2003.

[17] H. A. Macleod, *Thin Film Optical Filters*, 3rd ed. Bristol, PA: Inst. Phys., 2001.

[18] B. Wolf, *Principles of Optics*, 5th ed. Cambridge, U.K.: Cambridge Univ. Press, 1991.

[19] E. Stoykova, "Transmission of a Gaussian beam by a Fizeau interferential wedge," *J. Opt. Soc. Amer. A, Opt. Image Sci.*, vol. 22, no. 12, pp. 2756–2765, Dec. 2005.

[20] A. Holke and H. T. Henderson, "Ultra-deep anisotropic etching of (110) silicon," *J. Micromech. Microeng.*, vol. 9, no. 1, pp. 51–57, 1999.

[21] S. S.-S. Yun, "Fabrication of vertical optical plane using DRIE and KOH crystalline etching of (1 1 0) silicon wafer," *Sens. Actuators. A, Phys.*, vol. 128, no. 2, pp. 387–394, 2006.

Ariel Lipson received the B.Eng. and M.Sc. degrees in electrical engineering from the Technion Institute of Technology, Haifa, Israel, in 1998 and 2001, respectively, and the Ph.D. degree from the Imperial College London, London, U.K.

He is currently with Microsaic Systems Ltd., Surrey, U.K. He was with Intel Research Centre, Haifa, between 1995 and 1998 and co-founded a biotechnological company in 2000. His scientific interests are in the field of optical communications and integrated optics, MEMS and microsystems, and biosensors.

Eric M. Yeatman received the B.Eng. degree in engineering physics and the M.Sc. degree in physics from Dalhousie University, Halifax, NS, Canada, in 1985 and 1986, respectively, and the Ph.D. degree from the Imperial College London, London, U.K., in 1989.

Since 1989, he has been a member of staff in the Optical and Semiconductor Devices Group, Department of Electrical and Electronic Engineering, Imperial College London, as the Deputy Head of Group since 1996 and as a Professor of Microengineering since 2005. His current research includes micromechanical actuators and generators, microstructures for optical and microwave applications, and integrated optical amplifiers.